On Bubble Rings and Ink Chandeliers

MARCEL PADILLA, TU Berlin
ALBERT CHERN, TU Berlin
FELIX KNÖPPEL, TU Berlin
ULRICH PINKALL, TU Berlin
PETER SCHRÖDER, Caltech

We introduce variable thickness, viscous vortex filaments. These can model such varied phenomena as underwater bubble rings or the intricate "chandeliers" formed by ink dropping into fluid. Treating the evolution of such filaments as an instance of Newtonian dynamics on a Riemannian configuration manifold we are able to extend classical work in the dynamics of vortex filaments through inclusion of viscous drag forces. The latter must be accounted for in low Reynolds number flows where they lead to significant variations in filament thickness and form an essential part of the observed dynamics. We develop and document both the underlying theory and associated practical numerical algorithms.

CCS Concepts: • **Mathematics of computing → Partial differential equations**; *Differential calculus*; *Algebraic topology*; • **Computing methodologies → Mesh models**; *Physical simulation*; • **Applied computing →** *Physics*.

Additional Key Words and Phrases: Differential geometry, physical modeling, geodesics, fluid simulation, vorticity methods, vortex filaments.

ACM Reference Format:
Marcel Padilla, Albert Chern, Felix Knöppel, Ulrich Pinkall, and Peter Schröder. 2019. On Bubble Rings and Ink Chandeliers. *ACM Trans. Graph.* 38, 4, Article 129 (July 2019), 14 pages. https://doi.org/10.1145/3306346.3322962

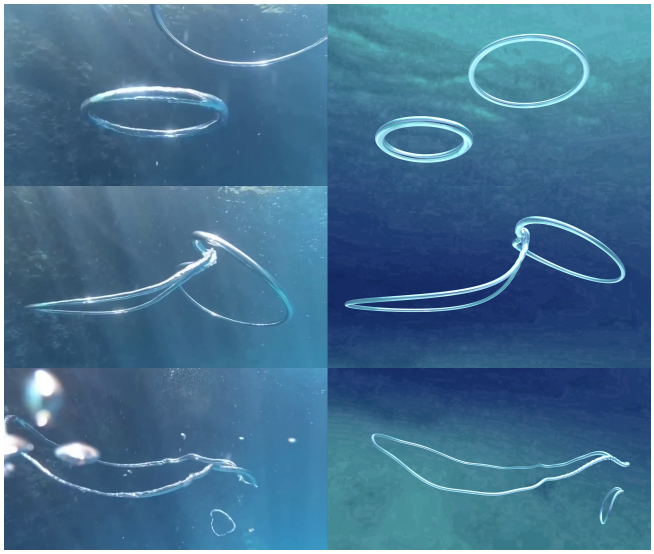

Fig. 1. Evolution of two underwater bubble rings connecting, showing frames from a video (left) and our simulation (right) with approximate ring size 2 m and circulation 2.5 $m^2\,s^{-1}$. See also the video at time 1:12.

1 INTRODUCTION

The study of vortex dynamics is by now a classical subject in fluid dynamics [Saffman 1992] with roots all the way back to Cauchy [1815] (see [Frisch and Villone 2014] for an historical account). One of the central elements in this study is the vortex filament, first articulated by Helmholtz [1858] (see [Meleshko et al. 2012] for an historical account). A vortex filament is a closed curve (or beginning and ending on the boundary of the domain) carrying concentrated vorticity, generating a velocity field according to the Biot–Savart law [1820]. Vortex filaments are easily accessible through experiment [Rogers 1858], serve as useful abstractions in the analysis of flows [Shariff and Leonard 1992], and can serve as a basis for Lagrangian flow simulations in the high Reynolds number regime in computational fluid dynamics and computer graphics [Chorin 1990, 1993; Angelidis and Neyret 2005; Bernard 2006, 2009; Weißmann and Pinkall 2010; Liao et al. 2018] (to name but a few).

Comparatively less is known about the evolution of vortex filaments in low to moderate Reynolds number flows, where they can model beautiful phenomena as diverse as bubble rings [Turner 1957; Pedley 1968] (Figs. 1, 3) and the chandeliers formed by ink dropping into clear fluid [Tomlinson 1864; Thomson and Newall 1886] (Figs. 2, 4). In these settings viscous drag and buoyancy affect thickness variations along the filament. These have significant impact on the dynamics of the filament as a whole and must be modeled explicitly.

To capture these dynamics we develop a model for variable thickness vortex filaments subject to viscous drag and buoyancy. The dynamics without drag and buoyancy coincide with classic descriptions [Moore and Saffman 1972] according to the Biot–Savart [1820] and Bernoulli [1738] laws. To account for the effect of dissipative drag we first recast the classic evolution equations as geodesic equations on a suitably constructed configuration manifold [Kaluza 1921; Klein 1926]. Dissipative drag can then be included in a standard manner (as can other external forces such as buoyancy). This results in three coupled equations describing the deformation of the center curve of the filament (Eq. (18)), changes in the thickness along the filament (Eq. (15)), and changes in the circulation, *i.e.*, filament strength (Eq. (12b)), as functions of time. Using appropriate numerical methods, which we detail, we demonstrate the fidelity of our model through simulations and comparisons with experiments.

Permission to make digital or hard copies of all or part of this work for personal or classroom use is granted without fee provided that copies are not made or distributed for profit or commercial advantage and that copies bear this notice and the full citation on the first page. Copyrights for components of this work owned by others than ACM must be honored. Abstracting with credit is permitted. To copy otherwise, or republish, to post on servers or to redistribute to lists, requires prior specific permission and/or a fee. Request permissions from permissions@acm.org.
© 2019 Association for Computing Machinery.
0730-0301/2019/7-ART129 $15.00
https://doi.org/10.1145/3306346.3322962

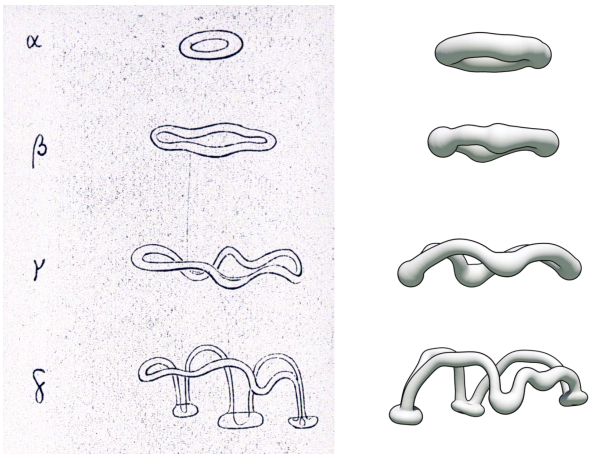

Fig. 2. Dynamic evolution of an ink drop showing Fig. 8 from [Thomson and Newall 1886] (left) and stills from a simulation (right), rendered with toon shading (*cf.* Fig. 4, right column). See also the video at 2:17.

1.1 Related Work

Much of the visual complexity of fluids arises from the distinction between different phases/materials: the interface between water and air, the flow of smoke in air, or the settling of particles in a suspension (to name but a few). Not surprisingly many different methods to capture phenomena of this type have been published in the computer graphics literature (see [Ren et al. 2018] for a recent, comprehensive review). None of these methods though model the vortex filament structures which describe the evolution of ink falling in water or a bubble ring rising under water. The former being an example of negative buoyancy in a low Reynolds number fluid, while the latter is one of positive buoyancy in a moderate Reynolds number fluid. In the fluid dynamics literature though there is considerable research devoted to these phenomena. Already in the late 19$^{\text{th}}$ century Tomlinson [1864] and Thomson and Newall [1886] described the intricate chandeliers formed by ink drops falling in a fluid. In particular they noted that the drops quickly form vortex filaments entraining the ink. These filaments subsequently develop uneven thickness due to the low Reynolds number nature of the flow. This leads to nucleation of the arms of the chandelier (Figs. 2, 4). Detailed study of their evolution is still the subject of ongoing work in both direct numerical simulation (Navier-Stokes on an Eulerian grid) and experiment [Shimokawa et al. 2016] (and references therein). But hitherto no explicit variable thickness vortex filament subject to dissipative drag and negative buoyancy has been developed, not withstanding the long history of increasingly refined vortex filament models [Widnall and Bliss 1971; Moore and Saffman 1972; Lundgren and Ashurst 1989; Marshall 1991], to name but a few.

Bubble rings are another example of buoyant vortex filaments, this time with positive buoyancy due to the air they contain and moving in a moderate Reynolds number environment. Research on bubble rings in the fluid dynamics literature goes back to the middle of the 20$^{\text{th}}$ century [Turner 1957; Pedley 1968] with theoretical development of detailed physical models and their analysis continuing to this day [Chang and Smith 2018] (and references therein). Similarly, the investigation of their behavior with direct numerical simulation (using boundary integral or lattice Boltzmann methods) [Lundgren and Mansour 1991; Cheng et al. 2013] is ongoing. Boundary integral methods have also been used in the computer graphics community for fluid phenomena fully characterized by the evolution of their bounding surface [Da et al. 2016], and could possibly be extended to model bubble rings. These surface methods are generalizations of vortex sheet approaches which have proven themselves useful at larger scales [Stock et al. 2008; Brochu et al. 2012; Pfaff et al. 2012; Da et al. 2015]. Since filaments are 1-dimensional structures they are more parsimonious for the task at hand yet no explicit mathematical model for the evolving geometry of a bubble ring as the variable thickness vortex filament it is, has hitherto been developed. 1-dimensional Lagrangian descriptions have also proven advantageous for viscous threads [Bergou et al. 2010]. There a highly viscous fluid fills the inside of a variable thickness filament while the physics are dominated by elastic forces rather than vorticity.

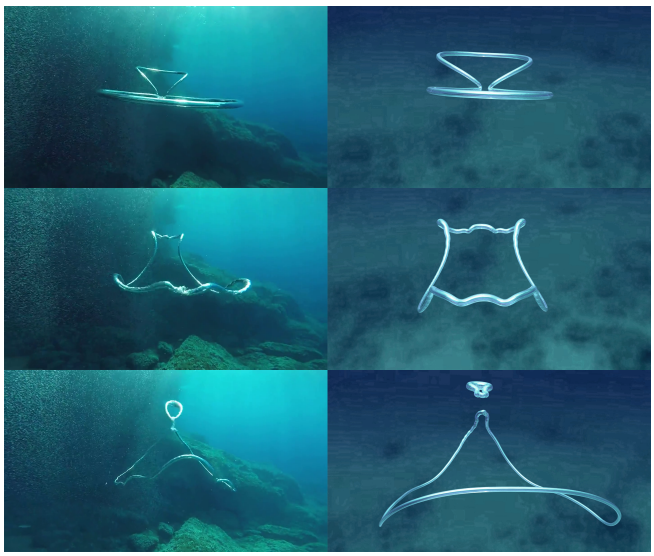

Fig. 3. Two bubble rings connecting with subsequent waves traveling along the single ring so violently that they cause a subsequent reconnection separating off a small bubble ring. Shown on the left are frames from a video, while the right shows frames from a simulation. The ring is approximately 2 m in diameter and 5.0 $\text{m}^2\,\text{s}^{-1}$ in circulation. See also the video at 1:37.

1.2 Our Approach

In this paper we develop a variable thickness, vortex filament, a descriptor we shorten to *filament* for the remainder of the paper. It will be subject to dissipative drag in a low to moderate ($\approx 1 - 500$) Reynolds number regime and driven by buoyancy (and possibly other forces).

We use filaments as primitives since they directly capture the geometry of the dominant phenomenon. The underlying assumption is that the filament is thin relative to its overall scale and its curvature radius larger than its thickness. Due to the small scale

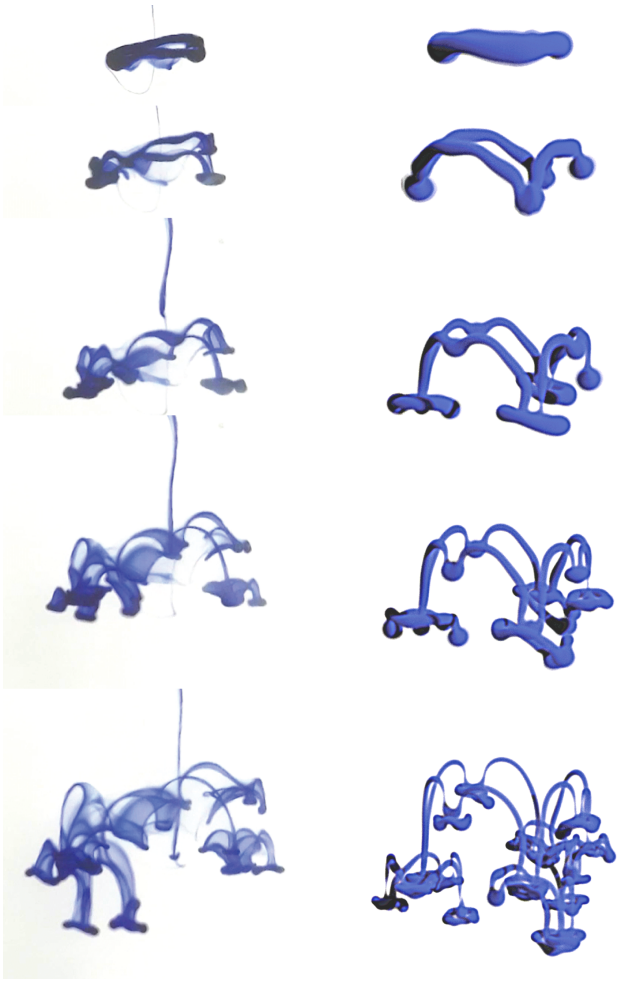

Fig. 4. A Thomson chandelier comparing video frames of an experiment (left) and a simulation (right), rendered with volume rendering (*cf.* Fig. 2, right column). The ring is approximately 1 cm in diameter. See also the video at 2:32.

of the filament thickness relative to the volume in which it moves, we assume the flow in the interior of the filament to be Stokes, *i.e.*, advective inertial forces are small compared with viscous forces. On the outside the flow is modeled as irrotational, *i.e.*, we assume that the filament is embedded in a large flow field with negligible boundary (shear) effects. Finally the fluid is assumed to be of uniform density and viscosity. When the density varies significantly we employ a Boussinesq approximation, *i.e.*, density differences appear only in terms involving gravity.

To derive the evolution laws for such a filament we first recall the Newtonian dynamics description of an evolving incompressible fluid with dissipation (the Navier-Stokes equations). In that point of view the configuration manifold of the fluid is given by the volume preserving diffeomorphisms [Arnold and Khesin 1998] and an Euler fluid evolves as a geodesic. For vortex sheets a formulation as geodesics on a suitable configuration manifold can be found in [Loeschke 2012] as well as [Izosimov and Khesin 2018]. Our task is to develop this machinery when the underlying configuration manifold is given by filaments.

To establish the general picture, we begin with a brief recall of fluids from the point of view of Newtonian dynamics on a Riemannian configuration manifold. Readers not familiar with Riemannian geometry can find relevant background material in [Gallot et al. 2004].

Table 1. Notation.

Notation	Meaning
$\gamma \in \mathcal{M} \subset C^\infty(\mathbb{S}^1, \mathbb{R}^3)$	filament configuration manifold
$T\mathcal{M}, T^*\mathcal{M}$	tangent bundle and its dual, the co-tangent bundle
$\langle \cdot, \cdot \rangle$	metric
$Y^\flat(\cdot) \coloneqq \langle Y, \cdot \rangle$	musical isomorphisms mapping vector fields Y to co-vector fields $Y^\flat$ and conversely mapping co-vector fields (1-forms) α to vector fields $\alpha^\sharp$
$\langle \alpha^\sharp, \cdot \rangle \coloneqq \alpha(\cdot)$	
$\dot\gamma, \mathring\gamma \in T_\gamma \mathcal{M}$	tangent vector at γ which is a velocity field along γ
$a \colon \mathbb{S}^1 \to \mathbb{R}^+$	positive radius of the filament
$A \coloneqq \pi a^2$	cross sectional area of filament
T	normalized tangent vector of γ
$\dot\gamma^\top \coloneqq \langle T, \dot\gamma \rangle T$	tangential and normal components along γ
$\dot\gamma^\perp \coloneqq \dot\gamma - \dot\gamma^\top$	
$\langle \dot\gamma, \mathring\gamma \rangle_{(1,2)} \coloneqq$ $\langle \dot\gamma^\top, \mathring\gamma^\top \rangle + 2\langle \dot\gamma^\perp, \mathring\gamma^\perp \rangle$	anisotropic inner product along γ
$I \colon T\mathcal{M} \to T^*\mathcal{M}$	positive definite inertia tensor mapping vectors to co-vectors
$\langle \cdot \vert \cdot \rangle \colon V^* \times V \to \mathbb{R}$	dual/primal pairing of co-vectors and vectors for a vector space V
$D \colon T\mathcal{M} \to T^*\mathcal{M}$	positive semi-definite drag tensor
$B \colon T\mathcal{M} \to T^*\mathcal{M}$	skew-adjoint "magnetic field" tensor
$\rho, \mu, \nu = \frac{\mu}{\rho}$	density, dynamic viscosity, and kinematic viscosity
$\nabla^{\mathcal{M}}, \nabla^{\widetilde{\mathcal{M}}}$	Levi-Civita connection (covariant derivative) on $\mathcal{M}$ & $\widetilde{\mathcal{M}}$
U, C, G, F	Biot–Savart energy of a unit strength filament, circulation, potential energy (*e.g.*, gravitational potential), and force
$u_{\mathrm{BS}} =: C\hat{u}_{\mathrm{BS}}$	velocity on γ due to the Biot–Savart field as the product of strength C and a unit strength filament velocity $\hat{u}_{\mathrm{BS}}$
$g_0 = (0, 0, -9.8)$	gravity vector
$\mathrm{At} \coloneqq \frac{\rho_1 - \rho_2}{\rho_1 + \rho_2}$	Atwood number: relative density difference ($\rho_1 > \rho_2$)

2 NEWTONIAN DYNAMICS OF FLUIDS

Let $\mathcal{M}$ be a configuration space equipped with a Riemannian metric $\langle\cdot,\cdot\rangle$. Given a point $\gamma \in \mathcal{M}$ and a velocity $\dot\gamma \in T_\gamma\mathcal{M}$ denote the kinetic energy as $\frac{1}{2}\langle\dot\gamma,\dot\gamma\rangle$. The metric induces a $\flat$-operator (one of the musical isomorphisms [Gallot et al. 2004, 2.B(2.66)]) mapping vectors to co-vectors. This is also called the inertia tensor $I\colon T\mathcal{M} \to T^*\mathcal{M}$ so that at each $\gamma \in \mathcal{M}$

$$\langle I\dot\gamma|\mathring{\dot\gamma}\rangle := \langle\dot\gamma,\mathring{\dot\gamma}\rangle, \quad \dot\gamma,\mathring{\dot\gamma} \in T_\gamma\mathcal{M}$$

and $I\dot\gamma$ becomes the momentum (co-vector) associated to a velocity (vector) $\dot\gamma \in T_\gamma M$. Here we use $\langle\cdot|\cdot\rangle$ to denote the pairing of dual and primal spaces of a vector space.

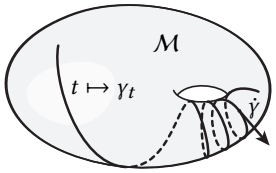

In the case of incompressible fluids $\mathcal{M} = \mathrm{SDiff}(M)$ is the Lie-group of volume preserving diffeomorphisms $\gamma\colon M \to M$ of the fluid domain $M \subseteq \mathbb{R}^3$ to itself [Arnold and Khesin 1998]. Its tangent spaces are the divergence free (no production or loss) vector fields $u\colon M \to \mathbb{R}^3$ tangent to the boundary with normal N (no particles traveling through the wall)

$$T_\gamma\mathcal{M} = \{\dot\gamma = u\circ\gamma \mid \operatorname{div} u = 0, \langle u, N\rangle = 0\}\,.$$

The kinetic energy of a divergence free velocity field $\dot\gamma \in T_\gamma\mathcal{M}$ derives from its squared L^2-norm

$$E(\dot\gamma) = \frac{\rho}{2}\int_M |\dot\gamma|^2 = \frac{\rho}{2}\int_M |u|^2$$

where ρ denotes the density.

Returning to the general case, we note that a Riemannian manifold has a unique Levi-Civita connection $\nabla^{\mathcal{M}}$ (covariant derivative compatible with the metric and torsion free [Gallot et al. 2004, 2.B]). The acceleration $\ddot\gamma$ of a trajectory $t \mapsto \gamma_t$ is then

$$\ddot\gamma = \nabla^{\mathcal{M}}_{\dot\gamma_t}\dot\gamma.$$

Here we see that in the Riemannian setting the 2nd time derivative involves the covariant derivative, since we need to differentiate a tangent vector field (velocity) along a path (time evolution) in a Riemannian manifold. Newton's Law of Motion can now be stated as follows. Suppose $F_t \in T^*_{\gamma_t}\mathcal{M}$ is a given net force (co-vector) along the trajectory $t \mapsto \gamma_t$ then

$$I\ddot\gamma = F.$$

For $F = 0$ we get geodesic ("straightest") motion.

Returning to incompressible fluids, geodesic motion, *i.e.*, time evolution of the fluid field without any forces acting on it, gives rise to the Euler equations in Lagrangian form on vector fields [Arnold and Khesin 1998]

$$\nabla^{\mathcal{M}}_{\dot\gamma_t}\dot\gamma = \left(\frac{\partial u}{\partial t} + \nabla^{\mathbb{R}^3}_u u + \operatorname{grad}\frac{p}{\rho}\right)\circ\gamma = 0. \tag{1}$$

The first two terms in the middle are the usual material derivative in the space of all diffeomorphisms, $\mathrm{Diff}(M) \supset \mathcal{M}$. The third term is the projection of the material derivative back to $T_\gamma\mathcal{M}$, *i.e.*, the tangent space to the submanifold of volume preserving diffeomorphisms. Taken together these three terms yield the Levi-Civita connection $\nabla^{\mathcal{M}}$ [Gallot et al. 2004, 2.B.2]. Physically the projection can be seen as a "pressure projection," ensuring a divergence free vector field.

Important examples of forces F in the general setting are those due to a potential energy $G\colon \mathcal{M} \to \mathbb{R}$, $F = -dG$, and drag forces due to dissipation. In a linear theory, the drag force is given by $-D\dot\gamma$ where $D\colon T\mathcal{M} \to T^*\mathcal{M}$ is a self-adjoint positive semi-definite tensor. A typical Newtonian dynamical system then takes the form

$$I\ddot\gamma = -D\dot\gamma - dG. \tag{2}$$

In the case of incompressible fluids, the addition of dissipation yields the Navier-Stokes equations in vector form

$$\nabla^{\mathcal{M}}_{\dot\gamma_t}\dot\gamma = \nu(\Delta u)\circ\gamma \tag{3}$$

where $\nu = \frac{\mu}{\rho}$ is the kinematic viscosity and Δ the negative definite Laplacian.

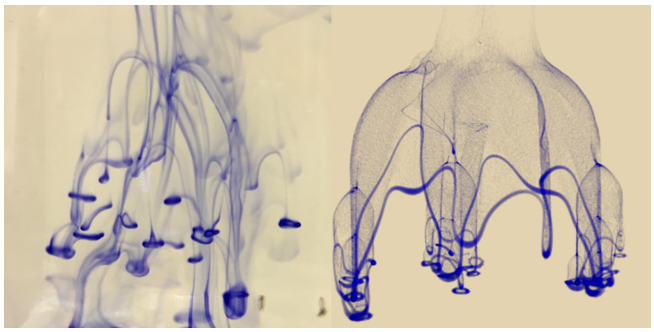

Fig. 5. Details of Thomson chandelier from experiment (left) and simulation (right). The structure is approximately 5 cm in size.

2.1 Roadmap

Here is how we will apply these ideas to derive equations of motion for filaments: First, we define the configuration space $\mathcal{M}$ for filaments (Sec. 3.1). The geometry of $\mathcal{M}$ will be independent of the circulation C, *i.e.*, the strength of the filaments. Defining the velocity field generated by the filaments, which does depend on C, we then compute their kinetic energy, using the metric on $\mathcal{M}$ and a potential energy term (Sec. 3.2). The forces acting on filaments due to circulation are stated next (Sec. 3.3). The resulting equations of motion are not geodesic with respect to the metric on $\mathcal{M}$. This motivates us to extend $\mathcal{M}$ by one dimension to a configuration space $\widetilde{\mathcal{M}}$ on which the equations of motion are purely geodesic (Sec. 3.4). Subsequently we complete our evolution model with drag and buoyancy as in Eq. (2). Analyzing these equations we arrive at first order differential equations for filament velocity, thickness, and circulation (Sec. 4).

3 VORTEX FILAMENTS WITH VARYING THICKNESS

3.1 Filament Geometry

A filament is an embedded closed curve $\gamma\colon \mathbb{S}^1 \to \mathbb{R}^3$ where $\mathbb{S}^1$ is some oriented 1-manifold diffeomorphic to the unit circle. (For now we consider only a single filament, though we will allow for multiple connected components each of which is diffeomorphic to the unit circle.) We denote the unit tangent of γ by $T\colon \mathbb{S}^1 \to \mathbb{S}^2 \subset \mathbb{R}^3$ and its arclength 1-form by ds, so that

$$d\gamma = T\,ds.$$

Filament thickness is given by a positive function $a\colon \mathbb{S}^1 \to \mathbb{R}^+$, with the filament interior M_1 swept out by circular disks of radius $a(s)$, centered at $\gamma(s)$ and orthogonal to $T(s)$ (Fig. 6). We assume

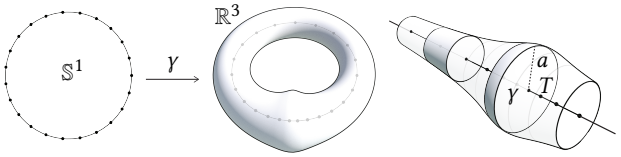

Fig. 6. Geometry of a variable thickness vortex filament described by its center curve γ together with a radius function $a > 0$. The full vortex filament is then the embedded solid torus swept out by disks of radius a normal to the tangent T along γ.

that $M = \mathbb{R}^3$ is filled with an incompressible fluid and distinguish between the interior M_1 of the filament and the exterior $M_0 = M \backslash M_1$. Filaments are assumed so thin that the mass contained in the portion of M_1 corresponding to any subset $U \subset \mathbb{S}^1$ is given by the integral over U of the 1-form

$$dm \coloneqq \rho \pi a^2 ds.$$

Since total mass is preserved, we let dm be a fixed 1-form on $\mathbb{S}^1$, something that can always be achieved for an evolving filament $t \mapsto \gamma_t$ by a suitable time-dependent reparameterization. Taken together this implies that the configuration space $\mathcal{M}$ of all filaments with given total ink mass is an open set

$$\mathcal{M} \subset C^\infty(\mathbb{S}^1, \mathbb{R}^3),$$

consisting of all embeddings $\gamma\colon \mathbb{S}^1 \to \mathbb{R}^3$ with a tube around γ of radius $a = (\frac{dm}{\rho \pi ds})^{1/2}$ yielding a smoothly embedded full torus.

3.2 Velocity Field Model

Given a variable thickness filament $\gamma \in \mathcal{M}$ we assume that all vorticity is contained in the filament interior M_1, where the flow is Stokes. In the exterior M_0 the velocity field is harmonic with a circulation around γ dictated by the vorticity inside M_1 and at rest at infinity. Demanding that both fields are continuous across the boundary ∂M_1 fixes the field $u(\dot\gamma, C)\colon \mathbb{R}^3 \to \mathbb{R}^3$ uniquely (App. E) as a function of the filament γ, its deformation $\dot\gamma$, and its strength parameter (circulation C).

The kinetic energy of u can be written as the sum of a "linear" component due to motion of γ, and a "rotational" component due to circulation

$$\begin{aligned} 2E(\dot\gamma, C) &\coloneqq \rho \int_{\mathbb{R}^3} |u(\dot\gamma, C)|^2 \\ &= \rho \int_{\mathbb{R}^3} |u(\dot\gamma, 0)|^2 + \rho \int_{\mathbb{R}^3} |u(0, C)|^2. \end{aligned}$$

For now we assume ρ to be the same throughout M, but will distinguish different densities in M_1 and M_0 later.

This decomposition relies on the approximate L^2-orthogonality of $u(\dot\gamma, 0)$ and $u(0, C)$ for thin filaments. To see this, first consider the interior M_1 in a plane orthogonal to the tangent vector of γ. There, to first order, $u(\dot\gamma, 0)$ is a dipole while $u(0, C)$ is a monopole, which are L^2 orthogonal (Fig. 9; left & center). For the exterior M_0 note that $u(\dot\gamma, 0)$ gives rise to the gradient of a potential, while $u(0, C)$ is divergence free and tangential to the boundary of the filament. Application of Green's first identity then yields the vanishing of their L^2 inner product.

The first summand defines the inertia tensor on $\mathcal{M}$ (App. B.2)

$$\langle I\dot\gamma | \dot\gamma \rangle \coloneqq \rho \int_{\mathbb{R}^3} |u(\dot\gamma, 0)|^2 = \frac{4}{3} \int_{\mathbb{S}^1} |\dot\gamma|^2_{(1,2)} dm \tag{4}$$

through $|\dot\gamma|^2_{(1,2)} \coloneqq |\dot\gamma^\top|^2 + 2|\dot\gamma^\perp|^2$ which weighs tangential $\dot\gamma^\top \coloneqq \langle \dot\gamma, T \rangle T$ and normal $\dot\gamma^\perp \coloneqq \dot\gamma - \dot\gamma^\top$ directions along γ differently. The higher weight in the normal direction is not surprising once one considers that tangential motion requires less work than normal motion.

The second summand is quadratic in C and is well approximated for thin filaments by the Biot–Savart kinetic energy (App. B.2.1)

$$\rho \int_{\mathbb{R}^3} |u(0, C)|^2 \approx 2C^2 U \tag{5}$$

where U denotes the Biot–Savart energy of a unit strength filament of shape γ (App. B.1.1). Together the two summands give us the overall kinetic energy

$$E(\dot\gamma, C) = \tfrac{1}{2} \langle I\dot\gamma | \dot\gamma \rangle + C^2 U \tag{6}$$

with C as a constant parameter of our model.

3.3 Equations of Motion

The forces acting on a variable thickness filament are given by Moore and Saffman [1972, Eq. 5.19] (App. C) as

$$F = \rho C T \times (\dot\gamma - u_{\mathrm{BS}}) ds - \frac{\rho C^2}{4\pi} \frac{da}{a} T, \tag{7}$$

where $u_{\mathrm{BS}}\colon \mathbb{S}^1 \to \mathbb{R}^3$ is the Biot–Savart velocity generated by the filament, acting on the filament. The first term is the Kutta-Joukowski lift force [Saffman 1992, § 3.1] (normal to the filament) proportional to the relative velocity of the filament. The second term is due to thickness variations (tangential to the filament). When these forces are in balance ($F = 0$), vanishing of the normal component implies $\dot\gamma = u_{\mathrm{BS}}$. Vanishing of the tangential component implies $a = \text{const}$. This characterizes the classical setting where velocity is due only to the Biot–Savart law and thickness is constant along the filament (though variable in time). Conversely, additional forces such as buoyancy and dissipation will make the lifting term and thickness variations relevant, taking us beyond the classical setting.

By gathering terms linear or quadratic in C we can rewrite the force to reveal a deeper structure which will lead us to geodesic equations (Sec. 3.4). To wit

$$\begin{aligned} I\ddot\gamma &= \rho C T \times (\dot\gamma - u_{\mathrm{BS}}) ds - \frac{\rho C^2}{4\pi} \frac{da}{a} T \\ &= C\left(\rho T \times \dot\gamma ds\right) - C^2 \left(\rho T \times \hat u_{\mathrm{BS}} ds + \frac{\rho}{4\pi} \frac{da}{a} T\right) \\ &= -CB\dot\gamma - C^2 dU \end{aligned} \tag{8}$$

using $u_{\mathrm{BS}} =: C\hat u_{\mathrm{BS}}$, defining the skew-adjoint tensor $B\colon T\mathcal{M} \to T^*\mathcal{M}$, which acts like a magnetic field, and noting that the term proportional to C^2 is the differential of the normalized Biot–Savart energy U (App. B.1.1). In other words, the Biot–Savart energy C^2U acts here as if it were a potential energy when in fact it is a kinetic

energy (*cf.* Eq. (6)). The left-hand side of Eq. (8) involves the Levi-Civita connection $\nabla^{\mathcal{M}}$ since $\ddot{\gamma} = \nabla^{\mathcal{M}}_{\partial_t}\dot{\gamma}$. The particulars of $\nabla^{\mathcal{M}}$ are unimportant since $I\ddot{\gamma}$ will be dropped later (Sec. 4.1).

Unfortunately Eq. (8) is not yet in the form needed to add viscous drag in a sensible way. A potential energy is not affected by viscous dissipation and hence does not interact with filament motion through drag forces. What we need is a setup where the Biot–Savart energy stored in the fluid circulation is part of the inertia, *i.e.*, we need a metric which incorporates U. To accomplish this we will extend $\mathcal{M}$ by an extra dimension. In this added dimension, the velocity component of such an extended filament $\tilde{\gamma}$ will represent the circulation around the filament γ.

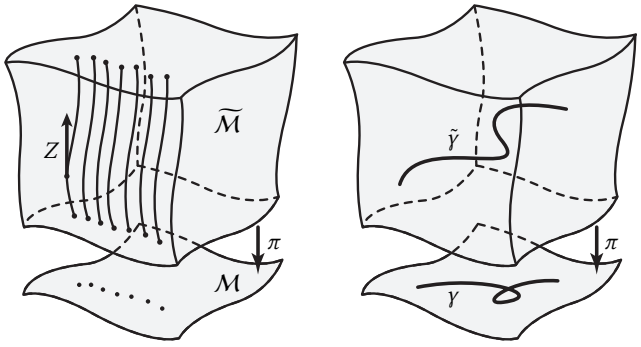

Fig. 7. We extend $\mathcal{M}$ through an additional ("vertical") dimension into $\widetilde{\mathcal{M}}$ in such a manner that geodesic paths $\tilde{\gamma} \in \widetilde{\mathcal{M}}$ project to paths $\pi \circ \tilde{\gamma} = \gamma \in \mathcal{M}$ which satisfy the filament equations of motion Eq. (8) (Sec. 3.3). The tangent vector field Z along the vertical direction captures the additional circulation parameter.

3.4 Filament Motion is Geodesic

In the absence of drag and gravity, filament motion can be viewed as geodesic motion on a Riemannian manifold $\widetilde{\mathcal{M}}$, constructed from $\mathcal{M}$ by adding one more dimension (App. A, Fig. 7).

The manifold $\widetilde{\mathcal{M}}$ comes with a projection map $\pi\colon \widetilde{\mathcal{M}} \to \mathcal{M}$ and a vector field Z. For a curve $\tilde{\gamma}\colon \mathbb{R} \to \widetilde{\mathcal{M}}$ we can then define the circulation by the scalar product

$$C = \langle \dot{\tilde{\gamma}}, Z \rangle.$$

For notational convenience we split the tangent spaces as $T_{\tilde{\gamma}}\widetilde{\mathcal{M}} = Z^{\perp} \oplus \mathbb{R}Z$ representing tangent vectors $\dot{\tilde{\gamma}} \in T_{\tilde{\gamma}}\widetilde{\mathcal{M}}$ as pairs $(\dot{\gamma}, C) \in T_{\gamma}\mathcal{M} \times \mathbb{R}$. The inertia tensor of $\widetilde{\mathcal{M}}$ is then written as

$$\tilde{I} = \begin{bmatrix} I & 0 \\ 0 & 2U \end{bmatrix}$$

so that the kinetic energy of $\tilde{\gamma}$ as a mass point equals the kinetic energy Eq. (6) of the velocity field corresponding to the filament $\gamma \coloneqq \pi \circ \tilde{\gamma}$ with circulation $C = \langle \dot{\tilde{\gamma}}, Z \rangle$

$$\tfrac{1}{2}\langle \tilde{I}\dot{\tilde{\gamma}} | \dot{\tilde{\gamma}} \rangle = \tfrac{1}{2}\langle I\dot{\gamma} | \dot{\gamma} \rangle + C^2 U.$$

With this construction $\tilde{\gamma}$ is geodesic if and only if C is constant and the filament γ moves according to Eq. (8)

$$\tilde{I}\ddot{\tilde{\gamma}} = \begin{pmatrix} I\ddot{\gamma} + CB\dot{\gamma} + C^2 dU \\ 2U\dot{C} \end{pmatrix} = \begin{pmatrix} 0 \\ 0 \end{pmatrix} \tag{9}$$

which is the co-vector version of Eq. (20) (App. A).

We are now ready to add viscous dissipation and gravity on $\widetilde{\mathcal{M}}$ to yield the complete evolution equations.

4 VORTEX FILAMENTS WITH DISSIPATION AND BUOYANCY

Viscous dissipation in the Navier-Stokes equations is $\mu(\Delta u) \circ \gamma$. Dealing with incompressible fluids, the dissipation is proportional to the squared L^2-norm of the curl of the velocity field defining a positive definite quadratic form $\widetilde{D}\colon T\widetilde{\mathcal{M}} \to T^*\widetilde{\mathcal{M}}$ (App. B)

$$\begin{aligned} \langle \widetilde{D}\dot{\tilde{\gamma}} | \dot{\tilde{\gamma}} \rangle &= \mu \int_{\mathbb{R}^3} |\operatorname{curl} u(\dot{\gamma}, C)|^2 \\ &= \mu \int_{\mathbb{R}^3} |\operatorname{curl} u(\dot{\gamma} - u_{\mathrm{BS}}, 0)|^2 + \mu \int_{\mathbb{R}^3} |\operatorname{curl} u(u_{\mathrm{BS}}, C)|^2 \\ &= 8\pi\mu \int_{\mathbb{S}^1} |\dot{\gamma} - u_{\mathrm{BS}}|^2_{(1,2)} ds + 4\pi\mu C^2 \int_{\mathbb{S}^1} \frac{1}{a^2} ds \end{aligned} \tag{10}$$

To incorporate gravity, define the potential

$$\widetilde{G} \coloneqq -\int_{\mathbb{S}^1} \langle \gamma, g \rangle dm \tag{11}$$

where $g \coloneqq \mathrm{A}t\, g_0$ is the effective gravity vector for g_0, the standard downward pointing gravity vector. For bubble rings the Atwood number (At) is -1 and for ink filaments $\frac{\rho_{\mathrm{ink}} - \rho}{\rho_{\mathrm{ink}} + \rho}$.

The final evolution equations are

$$\tilde{I}\ddot{\tilde{\gamma}} = -\widetilde{D}\dot{\tilde{\gamma}} - d\widetilde{G}$$

(*cf.* Eq. (2)) which are nothing other than the co-vector version of the Navier-Stokes equations Eq. (3) (with buoyancy) on our configuration manifold $\widetilde{\mathcal{M}}$. Unpacking all terms in this equation yields

$$\begin{aligned} I\ddot{\gamma} =& \rho C T \times (\dot{\gamma} - u_{\mathrm{BS}}) ds - \frac{\rho C^2}{4\pi} \frac{da}{a} T \\ &- 8\pi\mu(\dot{\gamma} - u_{\mathrm{BS}})^{\top} ds - 16\pi\mu(\dot{\gamma} - u_{\mathrm{BS}})^{\perp} ds \\ &+ \rho\pi a^2 g ds \end{aligned} \tag{12a}$$

$$2U\dot{C} = 8\pi\mu \int_{\mathbb{S}^1} \langle \hat{u}_{\mathrm{BS}}, \dot{\gamma} - u_{\mathrm{BS}} \rangle_{(1,2)} ds - 4\mu C \int_{\mathbb{S}^1} \frac{1}{a^2} ds \tag{12b}$$

using Eqs. (8), (11), and (21).

What about different densities? We have derived the inertia $\tilde{I}$ and dissipation tensor $\widetilde{D}$ assuming the same density in M_1 and M_0. Using the Atwood number for the buoyancy force we are using a Boussinesq approximation [Saffman 1992, Sec. 5.8]. This is reasonable for ink filaments, but less so for bubble rings. Whether accounting for different densities and viscosities in M_1 and M_0, when computing the inertia and dissipation tensors, pays off, is unclear due to the thin filament assumption. We leave exploration of this issue to future work.

4.1 First Order Equations

To arrive at our final equations we set $I\ddot{\gamma} = 0$ in Eq. (12a) (and leave Eq. (12b) unchanged). We do so because $I\ddot{\gamma}$ goes to zero in the thin limit ($a \to 0$) while the right-hand side of Eq. (12a) grows without bound.

Dividing Eq. (12a) by ρds and using the kinematic viscosity $\nu = \frac{\mu}{\rho}$ we arrive at a first-order differential equation for γ

$$0 = (-16\pi\nu + CT\times)(\dot{\gamma} - u_{\mathrm{BS}})^{\perp} - 8\pi\nu(\dot{\gamma} - u_{\mathrm{BS}})^{\top} - \frac{C^2}{4\pi}\frac{1}{a}\frac{da}{ds}T + \pi a^2 g.$$

Using the fact that $(-16\pi\nu + CT\times)^{-1} = (256\pi^2\nu^2 + C^2)^{-1}(-16\pi\nu - CT\times)$ in the plane orthogonal to T, we split this equation into normal and tangential differential equations for γ

$$\dot{\gamma}^{\perp} = u_{\mathrm{BS}}^{\perp} + \frac{16\pi^2\nu a^2}{256\pi^2\nu^2 + C^2} g^{\perp} + \frac{\pi a^2 C}{256\pi^2\nu^2 + C^2} T \times g \tag{13a}$$

$$\dot{\gamma}^{\top} = u_{\mathrm{BS}}^{\top} - \frac{C^2}{32\pi^2\nu}\frac{1}{a}\frac{da}{ds}T + \frac{a^2}{8\nu} g^{\top}. \tag{13b}$$

4.2 Thickness Evolves under Burgers' Equation

To study the influence of the curve tangential flow on the thickness of the filament consider an evolution $\dot{\gamma}^{\perp} = 0$ and $\dot{\gamma}^{\top}$ without $u_{\mathrm{BS}}^{\top}$. Then the (scalar) speed v is given by

$$v = \frac{a^2}{8\nu}\langle g, T\rangle - \frac{C^2}{32\pi^2\nu}\frac{1}{a}\frac{da}{ds}. \tag{14}$$

This is an equation in Lagrangian coordinates. The domain of the variables a, γ, and ds is $\mathbb{S}^1$. The time derivative $\dot{\gamma}^{\perp}$ is with respect to a Lagrangian location and $d\dot{s}$ is generally non-zero. However $d\dot{m}$ is zero. Noting these facts we can translate the equation for the speed v into Eulerian form. Let ∂_t^E be the Eulerian partial derivative with respect to time. Then $\partial_t^E ds = 0$ and the conservation of volume $\pi a^2 ds$ can be written, using the Lie derivative $\mathcal{L}$, as

$$\partial_t^E(\pi a^2 ds) + \mathcal{L}_v(\pi a^2 ds) = 0.$$

As a conservation law this reads as

$$\partial_t^E(\pi a^2) + \partial_s(\pi a^2 v) = 0.$$

Substituting Eq. (14) and defining the cross sectional area $A := \pi a^2$ we obtain

$$\partial_t^E A + \partial_s\left(\frac{\langle g, T\rangle}{8\pi\nu}A^2\right) = \frac{C^2}{64\pi^2\nu}\partial_s^2 A. \tag{15}$$

This is a viscous Burgers' equation [Bateman 1915; Burgers 1948] (see also [Whitham 1974, Ch. 4]).

4.3 Equilibrium Thickness

It is instructive to see what happens to the thickness evolution in the vanishing viscosity limit, *i.e.*, $\nu \to 0$. In the Burgers' equation this is equivalent to rescaling time so as to reach the steady state

$$\partial_s\left(\frac{\langle g, T\rangle}{8\pi}A^2\right) = \frac{C^2}{64\pi^2}\partial_s^2 A.$$

Integrating s once and noting that the integration constant vanishes since we are dealing with a periodic domain, we find that the steady state of the cross-sectional area A satisfies a Bernoulli differential equation [Hairer et al. 1993, Ch. I.3, Ex. 7]

$$\partial_s A = \frac{8\pi}{C^2}\langle g, T\rangle A^2. \tag{16}$$

This can be solved exactly in terms of the height (or depth) $z = \langle \frac{g}{|g|}, \gamma\rangle$ and an integration constant $z_0 \in \mathbb{R}$

$$|g|(z - z_0) = -\frac{C^2}{8\pi A}. \tag{17}$$

That is, the cross-sectional area is inversely proportional to the depth shifted by some constant z_0 (Fig. 8). The latter is uniquely determined by the tube volume $\int_{\mathbb{S}^1} A\, ds$.

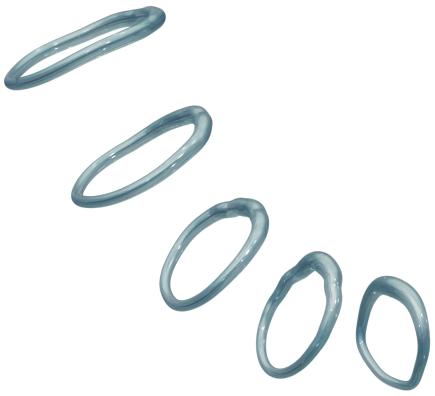

Fig. 8. A bubble ring starting in a vertical plane (lower right) is thicker towards the top. As it rises the ring grows and its symmetry plane turns more and more horizontal. The initial ring is 1 m in diameter, is 0.12 m in averaged thickness, and carries a circulation of 4.0 $\mathrm{m}^2\,\mathrm{s}^{-1}$. See also the video at 1:52.

Eq. (17) can also be understood as a pressure balance equation. The fluid pressure (up to an ambiant constant) at the filament tube surface is given by $-\frac{\rho}{2}(\frac{C}{2\pi a})^2$ according to Bernoulli's law applied to the vorticity-free tube exterior (App. C). This pressure is then balanced by the hydrostatic pressure $\rho|g|z$.

5 IMPLEMENTATION

Each filament γ is represented by a closed polygonal curve embedded in $\mathbb{R}^3$ with each edge annotated with a thickness variable a. The polygonal curve also carries a circulation variable C. Each edge is assigned its volume $V = \pi a^2 \Delta s$ where Δs is the length of the edge.

To stably evolve the filament by Eq. (13), we split the dynamics into two parts. In the first part we evolve the filament according to the Biot–Savart flow and the normal equation Eq. (13a)

$$\dot{\gamma} = u_{\mathrm{BS}} + \frac{16\pi^2\nu a^2}{256\pi^2\nu^2 + C^2} g^{\perp} + \frac{\pi a^2 C}{256\pi^2\nu^2 + C^2} T \times g, \tag{18}$$

together governing the deformation of the center curve γ. Note that the radius a appearing on the right-hand side of Eq. (18) can be computed from knowledge of the edge volume and the edge length which depends on the current position of the vertices of γ.

In the second part of the splitting the remaining tangential evolution is integrated

$$\dot{\gamma}^{\top} = -\frac{C^2}{32\pi^2\nu}\frac{1}{a}\frac{da}{ds}T + \frac{a^2}{8\nu} g^{\top}. \tag{19}$$

This equation does not change the shape of the curve and can be reduced to Burgers' equation for the cross sectional area $A = \pi a^2$ on a fixed curve (*cf.* Sec. 4.2, Eq. (15)).

This leads to the main integration algorithm (with details of the numerical implementation delegated to App. D):

Algorithm 1 Main algorithm

1: **for each** time step **do**
2: Evolve the vertices of γ by Eq. (18) with an ODE solver for Δt time span. ▷ App. D.1
3: Evolve $A = \pi a^2$ by the viscous Burgers' equation Eq. (15) for Δt time span. ▷ App. D.2
4: Evolve C with Eq. (12b). ▷ App. D.3
5: Resample and allow topological changes of γ. ▷ App. D.4
6: $t \leftarrow t + \Delta t$.
7: **end for**

6 EVALUATION

We have implemented the theory presented here using SideFX' Houdini 16.5 software for all simulations and visualizations shown. The complete implementation software, allowing replication of all examples from this paper, is available in the form of Houdini assets with example hip files in the ancillary material.

6.1 Performance

The method is quite fast since our filaments are polygons of moderate resolution. The ink simulations visualized in the right columns of Figs. 2 and 4 have around 40 to 600 edges depending on the frame number and the simulations take 0.037 s and 0.155 s per time step on a machine with a 4.2 GHz Intel Core i7. Similarly for the bubble ring simulations we find approximately 40 to 170 edges and computation times per time step between 0.038 s and 0.072 s.

6.2 Parameters

All physical parameters needed to control the simulations take on their real world values in SI units. These are the initial ring radius in meters (m), initial ring thickness in meters (m), initial ring circulation in $\mathrm{m}^2\,\mathrm{s}^{-1}$, Atwood number (dimensionless, At ≈ 0.01 for ink and At ≈ -1 for bubbles), kinematic viscosity of water $\nu \approx 10^{-6}\ \mathrm{m}^2\,\mathrm{s}^{-1}$, and the gravity vector $g_0 \approx (0, 0, -9.8)\ \mathrm{m\,s}^{-2}$.

6.2.1 Ink Chandeliers. When modeling ink the initial circulation C is not very important. A downward traveling ring with arbitrarily high C eventually has C dying down to a critical value after which the ring starts to expand more rapidly, the thickness distribution driven by Burgers' equation becomes unstable, and after a while secondary rings begin to form (Figs. 4, 5). Their circulations continue to evolve according to Eq. (12b) until they die down to their critical values again, setting the stage for the next generation of rings. The trails visible in Fig. 5 just mark the path traced out by the filament. They were added in order to more closely match the visual appearance of real ink.

6.2.2 Bubble Rings. These take place at a larger length scale, and therefore their circulation stays relatively constant over a long time period. In order to have stable bubble rings this circulation C has to be large enough. In this $C \gg \nu$ regime the remaining effect of ν is visible in the propagation speed of thickness features due to Burgers' equation (Figs. 1, 3, 8). In the limit of $C \to \infty$ the thickness becomes constant.

Achieving a reconnection event mimicking closely the real underwater footage required a few iterations of differing relative placement of the initial rings, but provided no additional challenges.

7 LIMITATIONS AND POSSIBLE REFINEMENTS

There are a number of refinements of our approach whose study would be valuable and we discuss them here.

In our model formulation we assume the same density and viscosity in M_1 and M_0. For ink filaments this, together with the Boussinesq approximation, is a standard assumption. For bubble rings it may pay off to account for the different density and viscosity in M_1 vs. M_0 when deriving the inertia and dissipation tensors. We note however that the current method works remarkably well even for bubble rings. When the circulation around bubble rings becomes small they break up due to surface tension effects [Da et al. 2016]. While surface tension forces could be added to our model, evolution after the breakup would require a Lagrangian primitive other than a closed curve. We leave this extension to future work.

In our implementation we work with a separate C for each filament component, following its own evolution equation Eq. (12b). Eq. (12a) then uses the Biot–Savart field generated by all components. It is possible to augment the Kaluza–Klein construction by adding a dimension for each filament component. This would result in a coupled evolution equation for the vector of C variables. It would be interesting to see whether this effort pays off.

Interaction between multiple components of the same filament (same C value) or between multiple filaments occurs only via the Biot–Savart field. Since the dipole-like field generated by additional filament motion is a short range field, this is a valid approximation. However, in situations like drop formation or reconnection it might be helpful to work with the full exterior velocity field. Relatedly, generating the full interior velocity field would be useful for advection. For this integral equation techniques may be useful [Lundgren and Mansour 1988, 1991; Da et al. 2016].

We believe that our drop formation model handles vorticity correctly by creating a new child ring. However, this does not seem to capture correctly the ink flow during drop formation. The ink connects parent and child ring, maintaining the impression of a connected ink filament. It would be desirable to develop a more sophisticated model for drop formation which treats ink and vorticity separately. A similar question arises regarding the formation of the faint ink domes. Right now these are produced in our simulations as trails of the filaments. A theory describing their creation (and an implementation of this theory) is as yet missing.

8 CONCLUSION AND OUTLOOK

In the present paper we developed a variable thickness, viscous vortex filament to model low to moderate Reynolds flow phenomena such as bubble rings and ink chandeliers. We derived the equations of motion, including viscous dissipation, from geodesic equations on a configuration manifold for filaments with variable circulation. To go beyond the classical descriptions of vortex filaments we used ideas of Kaluza and Klein to extend a given configuration manifold in such a way that a motion law with magnetic field becomes geodesic on the extended Riemannian manifold. Numerical simulations based

on these equations exhibit many of the phenomena observed in experiments with under water bubble rings of ink dropped in water.

There are many directions in which the physics modeled by these filaments can be refined (Sec. 7). For bubble rings inclusion of surface tension promises to provide a basis for modeling their eventual disintegration. In the case of ink filaments a physical model describing the traces of ink ("domes") left behind would be desirable, as would be a more complete description of the transition from drop to filament. More generally, it may also be possible to extend these algorithms to more general shapes beyond tori. A particularly interesting avenue for future research would be the application of the machinery of Kaluza and Klein to other physical systems which can be cast in the Riemannian setting. One could use it to add viscosity effects in the context of surface-only approaches [Loeschke 2012, Ch. 2], [Izosimov and Khesin 2018, Thm. 7.10], and [Lundgren and Mansour 1988; Da et al. 2015, 2016].

ACKNOWLEDGMENTS

This work was supported in part by the DFG Collaborative Research Center TRR 109 "Discretization in Geometry and Dynamics," the Caltech Center for Information Science & Technology, and the Einstein Foundation Berlin. Additional support was provided by SideFX software.

REFERENCES

Alexis Angelidis and Fabrice Neyret. 2005. Simulation of Smoke based on Vortex Filament Primitives. In *Proc. Symp. Comp. Anim.* ACM, 87–96.

Vladimir I. Arnold and Boris A. Khesin. 1998. *Topological Methods in Hydrodynamics.* Springer.

Harry Bateman. 1915. Some Recent Researches on the Motion of Fluids. *Mon. Weath. R.* 43, 4 (1915), 163–170.

Mikl'os Bergou, Basile Audoly, Etienne Vouga, Max Wardetzky, and Eitan Grinspun. 2010. Discrete Viscous Threads. *ACM Trans. Graph.* 29, 4 (2010), 116:1–10.

Peter S. Bernard. 2006. Turbulent Flow Properties of Large-scale Vortex Systems. *PNAS* 103, 27 (2006), 10174–10179.

Peter S. Bernard. 2009. Vortex Filament Simulation of the Turbulent Coflowing Jet. *Phys. Fluids* 21, 2 (2009).

Danielis Bernoulli. 1738. *Hydrodynamica, sive de viribus et motibus fluidorum commentarii.* Argentorati. For a modern account see also [Grattan-Guinness 2005] and [Darrigol and Frisch 2008].

Jean-Baptiste Biot and Nicolas-Pierre-Antoine Savart. 1820. Note sur le Magnétisme de la pile de Volta. *Annal. Chimie et Phys.* 15 (1820), 222–223.

Tyson Brochu, Todd Keeler, and Robert Bridson. 2012. Linear-Time Smoke Animation with Vortex Sheet Meshes. In *Proc. Symp. Comp. Anim.* Eurographics Assoc., 87–95.

J. M. Burgers. 1948. A Mathematical Model Illustrating the Theory of Turbulence. *Adv. Appl. Math.* 1 (1948), 171–199.

Augustin-Louis Cauchy. 1815. Théorie de la Propagation des Ondes a la Surface d'un Fluide Pesant d'une Profondeur Indéfinie. In *Oeuvres Complètes d'Augustin Cauchy.* Vol. 1. Imprimerie Royale. Presented to the French Academy in 1815 (publ. 1827).

Ching Chang and Stefan G. Llewellyn Smith. 2018. The Motion of a Buoyant Vortex Filament. *J. Fl. Mech.* 857 (2018), R1:1–13.

M. Cheng, J. Lou, and T. T. Lim. 2013. Motion of a Bubble Ring in a Viscous Fluid. *Phys. Fluids* 25, 6 (2013), 067104:1–19.

Stephen Childress. 2009. *An Introduction to Theoretical Fluid Dynamics.* AMS.

Alexandre Joel Chorin. 1990. Hairpin Removal in Vortex Interactions. *J. Comput. Phys.* 91, 1 (1990), 1–21.

Alexandre Joel Chorin. 1993. Hairpin Removal in Vortex Interactions II. *J. Comput. Phys.* 107, 1 (1993), 1–9.

Fang Da, Christopher Batty, Chris Wojtan, and Eitan Grinspun. 2015. Double Bubbles Sands Toil and Trouble: Discrete Circulation-Preserving Vortex Sheets for Soap Films and Foams. *ACM Trans. Graph.* 34, 4 (2015), 149:1–9.

Fang Da, David Hahn, Christopher Batty, Chris Wojtan, and Eitan Grinspun. 2016. Surface-Only Liquids. *ACM Trans. Graph.* 35, 4 (2016), 78:1–12.

O. Darrigol and U. Frisch. 2008. From Newton's Mechanics to Euler's Equations. *Phy. D: Nonl. Phenom.* 237, 14–17 (2008), 1855–1869.

Uriel Frisch and Barbara Villone. 2014. Cauchy's almost Forgotten Lagrangian Formulation of the Euler Equation for 3D Incompressible Flow. *Eu. Phy. J. H* 39, 3 (2014), 325–351.

Sylvestre Gallot, Dominique Hulin, and Jacques Lafontaine. 2004. *Riemannian Geometry* (3rd ed.). Springer.

S. K. Godunov. 1959. A Difference Method for Numerical Calculation of Discontinuous Solutions of the Equations of Hydrodynamics. *Mat. Sb. (N.S.)* 47(89), 3 (1959), 271–306.

Ivor Grattan-Guinness (Ed.). 2005. *Landmark Writings in Western Mathematics 1640–1940.* Elsevier, Chapter Daniel Bernoulli: Hydrodynamica (G. K. Mikhailov), 131–142.

Ernst Hairer, Syvert Paul Nørsett, and Gerhard Wanner. 1993. *Solving Ordinary Differential Equations I: Nonstiff Problems* (2nd ed.). Springer.

Anton Izosimov and Boris Khesin. 2018. Vortex Sheets and Diffeomorphism Groupoids. *Adv. Math.* 338 (2018), 447–501.

Theodor Kaluza. 1921. Zum Unitätsproblem der Physik. *Sitzungsber. Preuss. Akad. Wiss. Berlin* (1921), 966–972. English translation in https://doi.org/10.1142/S0218271818700017.

Oskar Klein. 1926. Quantentheorie und Fünfdimensionale Relativitätstheorie. *Z. für Phys.* 37, 12 (1926), 895–906.

Eric Lauga and Thomas R. Powers. 2009. The Hydrodynamics of Swimming Microorganisms. *Rep. Prog. Phys.* 72 (2009), 096601:1–36.

Randall J. LeVeque. 2002. *Finite-Volume Methods for Hyperbolic Problems.* Cam. U. P.

Xiangyun Liao, Weixin Si, Zhiyong Yuan, Hanqiu Sun, Jing Qin, Qiong Wang, and Pheng-Ann Heng. 2018. Animating Wall-Bounded Turbulent Smoke via Filament-Mesh Particle-Particle Method. *IEEE Trans. Vis. Comp. Graph.* 24, 3 (2018), 1260–1273.

Christian Loeschke. 2012. *On the Relaxation of a Variational Principle for the Motion of a Vortex Sheet in Perfect Fluid.* Ph.D. Dissertation. Rhein. Fried.-Wilh.-Univ. Bonn.

T. S. Lundgren and W. T. Ashurst. 1989. Area-Varying Waves on Curved Vortex Tuibes with Application to Vortex Breakdown. *J. Fl. Mech.* 200 (1989), 283–307.

T. S. Lundgren and N. N. Mansour. 1988. Oscillations of Drops in Zero Gravity with Weak Viscous Effects. *J. Fl. Mech.* 194 (1988), 479–510.

T. S. Lundgren and N. N. Mansour. 1991. Vortex Ring Bubbles. *J. Fl. Mech.* 224 (1991), 177–196.

Jerrold Marsden and Alan Weinstein. 1983. Coadjoint Orbits, Vortices and Clebsch Variables for Incompressible Fluids. *Phy. D: Nonl. Phenom.* 7, 1–3 (1983), 305–323.

J. S. Marshall. 1991. A General Theory of Curved Vortices with Circular Cross-Section and Varialbe Core Area. *J. Fl. Mech.* 229 (1991), 311–338.

V. V. Meleshko, A. A. Gourjii, and T. S. Krasnopolskaya. 2012. Vortex Rings: History and State of the Art. *J. Math. Sc.* 187, 6 (2012), 772–808.

Derek William Moore and Philip Geoffrey Saffman. 1972. The Motion of a Vortex Filament with Axial Flow. *Phil. Tr. R. Soc. Lond. A* 272, 1226 (1972), 403–429.

T. J. Pedley. 1968. The Toroidal Bubble. *J. Fl. Mech.* 32, 1 (1968), 97–112.

Tobias Pfaff, Nils Thuerey, and Markus Gross. 2012. Lagrangian Vortex Sheets for Animating Fluids. *ACM Trans. Graph.* 31, 4 (2012), 112:1–8.

Bo Ren, Xu-Yun Yang, Ming C. Lin, Nils Thuerey, Matthias Teschner, and Chenfeng Li. 2018. Visual Simulation of Multiple Fluids in Computer Graphics: A State-of-the-Art Report. *J. Comp. Sc. Tech.* 33, 3 (2018), 431–451.

William B. Rogers. 1858. On the Formation of Rotating Rings by Air and Liquids under certain Conditions of Discharge. *Am. J. Sc. A.* 26, 77 (1858), 246–258.

Louis Rosenhead and Harold Jeffreys. 1930. The Spread of Vorticity in the Wake behind a Cylinder. *Proc. R. Soc. Lond. A* 127, 806 (1930), 590–612.

P. G. Saffman. 1992. *Vortex Dynamics.* Cam. U. P.

Karim Shariff and Anthony Leonard. 1992. Vortex Rings. *Ann. Rev. Fl. Mech.* 24 (1992), 235–279.

Michiko Shimokawa, Ryosei Mayumi, Taiki Nakamura, Toshiya Takami, and Hidetsugu Sakaguchi. 2016. Breakup and Deformation of a Droplet Falling in a Miscible Solution. *Phys. R. E* 93, 6 (2016), 062214:1–9.

Mark J. Stock, Werner J. A. Dahm, and Grétar Tryggvason. 2008. Impact of a Vortex Ring on a Density Interface using a Regularized Inviscid Vortex Sheet Method. *J. Comput. Phys.* 227, 21 (2008), 9021–9043. See also images at http://markjstock.com/#/chaoticescape/.

G. I. Taylor. 1953. Formation of a Vortex Ring by Giving an Impulse to a Circular Disk and then Dissolving it Away. *J. Appl. Ph.* 24, 1 (1953), 104–105.

J. J. Thomson. 1883. *A Treatise on the Motion of Vortex Rings.* Macmillan, London.

J. J. Thomson and H. F. Newall. 1886. On the Formation of Vortex Rings by Drops falling into Liquids, and some allied Phenomena. *Proc. R. Soc. Lond.* 39, 239–241 (1886), 417–436.

Charles Tomlinson. 1864. LXV. On a New Vareity of the Cohesion-Figures of Liquids. *Lon. Edin. Dub. Phil. M. J. Sc.* 27, 184 (1864), 425–432.

J. S. Turner. 1957. Buoyant Vortex Rings. *Proc. R. Soc. Lond. A* 239, 1216 (1957), 61–75.

Hermann von Helmholtz. 1858. Über Integrale der hydrodynamischen Gleichungen, welche den Wirbelbewegungen entsprechen. *J. Reine Angew. Math.* 55 (1858), 25–55.

Steffen Weißmann and Ulrich Pinkall. 2010. Filament-based Smoke with Vortex Shedding and Variational Reconnection. *ACM Trans. Graph.* 29, 4 (2010), 115:1–12.

G. B. Whitham. 1974. *Linear and Nonlinear Waves.* Wiley.

Sheila E. Widnall and Donald B. Bliss. 1971. Slender-body Analysis of the Motion and Stability of a Vortex Filament Containing an Axial Flow. *J. Fl. Mech.* 50, 2 (1971), 335–353.

A NON-RELATIVISTIC KALUZA-KLEIN

In the 1920's Kaluza [1921] and Klein [1926] proposed a construction unifying general relativity and electromagnetism by extending space-time with an extra dimension. In our non-relativistic context the analogous construction unifies electromagnetism with Newtonian mechanics. A particle γ with charge C traveling in a magnetic field B and subject to an electric potential U, can either be thought of as Newtonian mechanics with additional Lorentz and Coulomb forces (Eq. (8)), or as geodesic motion on a higher dimensional configuration space. Specifically, as claimed in Sec. 3.4, we can extend the Riemannian manifold $\mathcal{M}$ by one extra dimension to a Riemannian manifold $\widetilde{\mathcal{M}}$ in such a way that the solutions $t \mapsto \gamma_t \in \mathcal{M}$ of our equations of motion without gravity and drag (Eq. (8)) are the projections of geodesics $t \mapsto \tilde{\gamma}_t \in \widetilde{\mathcal{M}}$. In this section we construct $\widetilde{\mathcal{M}}$ explicitly.

As a manifold, $\widetilde{\mathcal{M}}$ is just the product $\widetilde{\mathcal{M}} = \mathcal{M} \times \mathbb{R}$ and the projection $\pi\colon \widetilde{\mathcal{M}} \to \mathcal{M}$ is just the projection onto the first factor. Note however that the projection $\theta\colon \widetilde{\mathcal{M}} \to \mathbb{R}$ onto the second factor (including the corresponding hypersurfaces $\theta = \text{const}$) will ultimately be irrelevant for the geometry of $\widetilde{\mathcal{M}}$. On the other hand, the vector field $Z := \partial_\theta$ will be important.

Our magnetic field $B\colon T\mathcal{M} \to T^*\mathcal{M}, \dot{\gamma} \mapsto -\rho T \times \dot{\gamma} ds$ from Eq. (8) arises from the Marsden-Weinstein [1983] 2-form β on $\mathcal{M}$

$$\beta(\dot{\gamma}, \mathring{\gamma}) := \rho \int_{\mathbb{S}^1} \det(d\gamma, \dot{\gamma}, \mathring{\gamma}),$$

as $-\iota_{\dot{\gamma}}\beta = -\rho T \times \dot{\gamma} ds$ (using $T ds = d\gamma$). Importantly, it is exact with $\beta = d\alpha$ for

$$\alpha(\dot{\gamma}) := \frac{\rho}{3} \int_{\mathbb{S}^1} \det(d\gamma, \gamma, \dot{\gamma}).$$

Then for each $\theta \in \mathbb{R}$, $\gamma \in \mathcal{M}$, $X \in T_\gamma \mathcal{M}$ we define a tangent vector

$$\widetilde{X} \in T_{(\gamma,\theta)}\widetilde{\mathcal{M}} = T_\gamma \mathcal{M} \oplus \mathbb{R} \quad \text{as} \quad \widetilde{X} := (X, -\alpha(X)).$$

For a function $f\colon \mathcal{M} \to \mathbb{R}$ the corresponding function on $\widetilde{\mathcal{M}}$ is defined as $\tilde{f} := f \circ \pi$. In other words we have defined the lifting map for tangent vectors and functions on $\mathcal{M}$ to those on $\widetilde{\mathcal{M}}$

Now we define a Riemannian metric on $\widetilde{\mathcal{M}}$ by setting for vector fields X, Y on $\mathcal{M}$

$$\langle \widetilde{X}, \widetilde{Y} \rangle := \langle X, Y \rangle \qquad \langle \widetilde{X}, Z \rangle := 0 \qquad \langle Z, Z \rangle := (2\widetilde{U})^{-1}.$$

Theorem A.1. *The Levi-Civita connection $\nabla^{\widetilde{\mathcal{M}}}$ of this Riemannian metric on $\widetilde{\mathcal{M}}$ is given by*

$$\nabla^{\widetilde{\mathcal{M}}}_{\widetilde{X}} \widetilde{Y} = \widetilde{\nabla^{\mathcal{M}}_X Y} - \tfrac{1}{2}\widetilde{\beta(X,Y)}Z \quad \textit{[Gallot et al. 2004, 3.D(3.55)]}$$
$$\nabla^{\widetilde{\mathcal{M}}}_{\widetilde{X}} Z = \nabla^{\widetilde{\mathcal{M}}}_Z \widetilde{X} = (4\widetilde{U})^{-1}\left(\widetilde{(BX)^\sharp} - 2\widetilde{dU(X)}Z\right)$$
$$\nabla^{\widetilde{\mathcal{M}}}_Z Z = (2\widetilde{U})^{-2}\widetilde{\operatorname{grad} U}.$$

Here $\sharp$ denotes the musical isomorphism mapping co-vectors to vectors [Gallot et al. 2004, 2.B(2.66)].

Proof. Since the vector fields $\widetilde{X}$ and $X = \pi_* \widetilde{X}$ are π-related, we have

$$\pi_*[\widetilde{X}, \widetilde{Y}] = [X, Y].$$

Moreover, $\widetilde{X}\theta = -\widetilde{\alpha(X)}$ and therefore

$$[\widetilde{X}, \widetilde{Y}]\theta = -\widetilde{X}\widetilde{\alpha(Y)} + \widetilde{Y}\widetilde{\alpha(X)} = -\widetilde{d\alpha(X,Y)} - \widetilde{\alpha([X,Y])}$$
$$\iff [\widetilde{X}, \widetilde{Y}] = \widetilde{[X,Y]} - \widetilde{\beta(X,Y)}Z$$

Similarly, one can check that for all vector fields X on $\mathcal{M}$ we have $[\widetilde{X}, Z] = 0$. Using these Lie brackets it is straightforward to verify that the above equations define an affine connection $\nabla^{\widetilde{\mathcal{M}}}$ on $\widetilde{\mathcal{M}}$ which is metric and torsion-free. □

For a path $t \mapsto \tilde{\gamma}_t = (\gamma_t, \theta_t)$ in $\widetilde{\mathcal{M}}$ we set

$$\dot{\tilde{\gamma}} =: \tilde{\dot{\gamma}} + C \cdot 2UZ.$$

In words: the velocity of the lift is the lift of the velocity plus additional terms ($C \cdot 2UZ$). Then $\tilde{\gamma}$ is a geodesic if and only if

$$0 = \nabla^{\widetilde{\mathcal{M}}}_{\partial_t} \dot{\tilde{\gamma}} = \left(\nabla^{\mathcal{M}}_{\partial_t}\dot{\gamma} + C(B\dot{\gamma})^\sharp + C^2 \operatorname{grad} U\right)^{\sim} + \dot{C} \cdot 2UZ \qquad (20)$$

which is equivalent to our equations of motion Eq. (9).

B MOVING FLUID TUBES

To compute the kinetic energy as well as the dissipation rate of the fluid field u on $\mathbb{R}^3$ induced by $(\gamma, \dot{\gamma}, C)$, we compute corresponding densities in slices orthogonal to the unit tangent T along γ. The filament is taken to have a disk cross section of radius $a > 0$ in each such slice and we construct corresponding divergence-free vector fields to explicitly calculate the energy ($\frac{1}{2}\|u\|^2$) and dissipation density ($\mu\|\omega\|^2$ for $\omega = \operatorname{curl} u$) per slice.

We distinguish three cases (Fig. 9): circulation only (no normal motion), normal translation (due to $\dot{\gamma}$), and pipeflow (tangential flow in the interior).

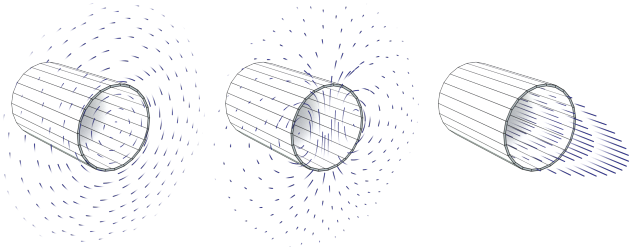

Fig. 9. We decompose a flow field into components induced by pure rotation (left), normal motion (middle), and interior tangential motion (right).

B.1 Circulation Only

In this case there is no motion within the slice and we only see a point vortex in the (x, y)-plane:

$$u_0(x, y) = \frac{C}{x^2 + y^2}\begin{pmatrix} -y \\ x \end{pmatrix} \qquad \text{for} \quad x^2 + y^2 \geq a^2.$$

The Stokes flow on the inside matching u on the boundary is just linear rotation (vanishing Laplacian)

$$u_1(x, y) = \frac{C}{a^2}\begin{pmatrix} -y \\ x \end{pmatrix} \qquad \text{for} \quad x^2 + y^2 \leq a^2.$$

Since we approximate the contribution of circulation to the kinetic energy of a filament (Eq. (5)) by the Biot–Savart energy (App. B.1.1), we only need the dissipation density per slice

$$\mu \int_{\mathbb{R}^2} |\omega|^2 = \mu \frac{4\pi}{a^2} C^2$$

B.1.1 Biot–Savart Energy and Velocity. The normalized Biot–Savart energy U of a variable thickness vortex filament can be written as the sum of the normalized Biot–Savart energy of a constant thickness (a_0) filament and a correction term

$$U = U^{(a_0)} + \frac{\rho}{4\pi} \int_{\mathbb{S}^1} \left(-\log \frac{a}{a_0} - \frac{1}{2} \right) ds$$
$$U^{(a_0)} = \frac{\rho}{8\pi} \int_{\mathbb{S}^1 \times \mathbb{S}^1} \frac{\langle T(s), T(\tilde{s}) \rangle}{\sqrt{|\gamma(s) - \gamma(\tilde{s})|^2 + \mu_{\mathrm{RM}}^2 a_0^2}} ds d\tilde{s} \quad \mu_{\mathrm{RM}} = e^{-3/4}.$$

This formula is based on the cut-off Biot–Savart integral introduced by Thomson [1883] and Rosenhead [1930] and elaborated in [Taylor 1953; Widnall and Bliss 1971; Moore and Saffman 1972] (see also [Saffman 1992, pp. 213]). The variations then follow as

$$dU(\dot{\gamma}) = \rho \int_{\mathbb{S}^1} \det(d\gamma, \hat{u}_{\mathrm{BS}}, \dot{\gamma}) + \frac{\rho}{4\pi} \int_{\mathbb{S}^1} \frac{da}{a} \langle T, \dot{\gamma} \rangle$$
$$\text{where} \quad \hat{u}_{\mathrm{BS}} = \hat{u}_{\mathrm{BS}}^{(a_0)} - \frac{1}{4\pi} \log \frac{a}{a_0} T \times \frac{dT}{ds}$$
$$\text{and} \quad \hat{u}_{\mathrm{BS}}^{(a_0)} = \frac{1}{4\pi} \int_{\mathbb{S}^1} \frac{T(\tilde{s}) \times (\gamma(s) - \gamma(\tilde{s}))}{\left(|\gamma(s) - \gamma(\tilde{s})|^2 + \mu_{\mathrm{RM}}^2 a_0^2 \right)^{3/2}} d\tilde{s}.$$

B.2 Normal Translation

This case has neither circulation nor interior flux, but the disk moves in the y-direction with speed v. A vector field u has a matching normal component on ∂M_1 if for $x^2 + y^2 = a^2$

$$vy = u_x x + u_y y.$$

This condition can be verified for the vector field

$$u_0(x, y) = \frac{va^2}{(x^2 + y^2)^2} \begin{pmatrix} 2xy \\ y^2 - x^2 \end{pmatrix} \qquad \text{for} \quad x^2 + y^2 \geq a^2.$$

This u_0 has the harmonic velocity potential

$$\phi(x, y) = -\frac{va^2}{x^2 + y^2} y.$$

The Stokes flow that extends this exterior velocity to the inside is

$$u_1(x, y) = \frac{v}{a^2} \begin{pmatrix} 2xy \\ -3x^2 - y^2 + 2a^2 \end{pmatrix} \qquad \text{for} \quad x^2 + y^2 \leq a^2.$$

One can directly verify that $\operatorname{div} u_1 = 0$ and

$$\operatorname{curl} u_1(x, y) = -\frac{8v}{a^2} x \qquad \Delta u_1(x, y) = -\frac{8v}{a^2} \begin{pmatrix} 0 \\ 1 \end{pmatrix}.$$

Since Δu_1 is a gradient vector field, u_1 is a Stokes flow and we get

$$\frac{\rho}{2} \int_{\mathbb{R}^2} |u|^2 = \frac{4}{3} \rho \pi a^2 v^2 \qquad \mu \int_{\mathbb{R}^2} |\omega|^2 = \mu 16 \pi v^2.$$

B.2.1 Remark. We are now also in a position to fully justify the approximation in Eq. (5). For thin filaments

$$2C^2 U = \rho \int_{\mathbb{R}^3} |u(u_{\mathrm{BS}}, C)|^2 = \rho \int_{\mathbb{R}^3} |u(u_{\mathrm{BS}}, 0)|^2 + |u(0, C)|^2$$
$$\approx \rho \int_{\mathbb{R}^3} |u(0, C)|^2$$

because the kinetic energy of normal displacements scales as a^2 while U scales as $\log a$ in the thin limit.

B.3 Interior Flux

Here we have zero velocity on the outside and we determine u_1 by prescribing the mean value v of the normal component of u_1. This leads to a quadratic velocity profile inside of the cylinder. For z the normal direction to the slice we get

$$u_1(x, y, z) = \frac{2v}{a^2} \begin{pmatrix} 0 \\ 0 \\ a^2 - x^2 - y^2 \end{pmatrix} \qquad \text{for} \quad x^2 + y^2 \leq a^2.$$

One can directly verify that $\operatorname{div} u_1 = 0$ and

$$\operatorname{curl} u_1(x, y, z) = -\frac{4v}{a^2} \begin{pmatrix} -y \\ x \\ 0 \end{pmatrix} \qquad \Delta u_1(x, y, z) = -\frac{8v}{a^2} \begin{pmatrix} 0 \\ 0 \\ 1 \end{pmatrix}.$$

Since Δu_1 is a gradient vector field, u_1 is a Stokes flow and we get

$$\frac{\rho}{2} \int_{\mathbb{R}^2} |u|^2 = \frac{2}{3} \rho \pi a^2 v^2 \qquad \mu \int_{\mathbb{R}^2} |\omega|^2 = \mu 8 \pi v^2.$$

B.4 Dissipation Tensor

From the above equations we get the entries of the drag tensor

$$\widetilde{D} = \begin{bmatrix} D_{11} & D_{12} \\ D_{12}^* & D_{22} \end{bmatrix}$$

as

$$D_{11} = 8\pi\mu \int_{\mathbb{S}^1} \langle \cdot, \cdot \rangle_{(1,2)} ds, \quad D_{12} = 8\pi\mu \int_{\mathbb{S}^1} \langle -\hat{u}_{\mathrm{BS}}, \cdot \rangle_{(1,2)} ds$$
$$D_{22} = 8\pi\mu \int_{\mathbb{S}^1} |\hat{u}_{\mathrm{BS}}|_{(1,2)}^2 ds + 4\pi\mu \int_{\mathbb{S}^1} \frac{1}{a^2} ds.$$

The drag force $-\widetilde{D}\dot{\gamma}$ is then

$$-\widetilde{D}\dot{\gamma} = \begin{pmatrix} -8\pi\mu(\dot{\gamma} - u_{\mathrm{BS}})^\top ds - 16\pi\mu(\dot{\gamma} - u_{\mathrm{BS}})^\perp ds \\ 8\pi\mu \int_{\mathbb{S}^1} \langle \hat{u}_{\mathrm{BS}}, \dot{\gamma} - u_{\mathrm{BS}} \rangle_{(1,2)} ds - 4\pi\mu C \int_{\mathbb{S}^1} \frac{1}{a^2} ds \end{pmatrix}. \quad (21)$$

C EQUATIONS OF MOTION: DERIVATION

Eq. (7) can be found in Moore and Saffman [1972, Eq. 5.19]. Here we give a brief derivation using only the Bernoulli (tangential force $F^\top$) and Biot–Savart (normal force $F^\perp$) laws.

Tangentially the (negative) pressure gradient acts along γ. Owing to the filaments being thin, rotation due to circulation will dominate the flow inside the filament. An inertial observer moving along with the filament will therefore mainly see a rigid rotation with a speed

$$u = \frac{C}{2\pi a}.$$

on the boundary ∂M_1. On the exterior M_0 such a co-moving observer will see an almost stationary vorticity-free flow, making Bernoulli's

law ($u^2/2 + p/\rho = \text{const}$) applicable. Taking its negative gradient we get

$$F^\top = \left(-\frac{\rho C^2}{4\pi^2 a^3}\frac{da}{ds}T\right)dm = -\frac{\rho C^2}{4\pi}\frac{da}{a}T.$$

For the normal force $F^\perp$ consider the continuous velocity field u_h which is harmonic in M_0, has circulation C around M_1, is Stokes inside M_1, and has zero normal velocity on ∂M_1. What does its vorticity $\omega_h = \operatorname{curl} u_h$ look like? Denote by ω_{BS} the uniform vorticity field inside of the filament M_1 with flux corresponding to the fixed circulation C. We cannot expect $\omega_h = \omega_{\mathrm{BS}}$ because the velocity field generated by ω_{BS}, the Biot–Savart field of γ, induces a non-trivial motion $u_{\mathrm{BS}} \colon \mathbb{S}^1 \to \mathbb{R}^3$ both along and orthogonal to the filament. In order to keep γ at rest we have to add to ω_{BS}, the vorticity of a dipole field (App. B.2) and a pipe flow (App. B.3), which together add a velocity $-u_{\mathrm{BS}}$, counter-balancing the motion of γ induced by ω_{BS}

$$\omega_h = \omega_{\mathrm{BS}} + \omega_{-u_{\mathrm{BS}}}.$$

In the presence of circulation and *non-vanishing* filament velocity $\dot\gamma$, the vorticity field will look like

$$\omega_h = \omega_{\mathrm{BS}} + \omega_{\dot\gamma - u_{\mathrm{BS}}}.$$

Inside the filament the velocity field corresponding to ω_h is just a rotation with angular velocity $\frac{C}{2\pi a^2}$ around the center curve. Neither the uniform vorticity field ω_{BS} nor the pipe flow vorticity are affected by this rotation. However, the dipole part of $\omega_{\dot\gamma - u_{\mathrm{BS}}}$ adds additional vorticity due to the rotation of the filament in which it "sits." In each small time increment Δt this amounts to

$$\Delta t \frac{C}{2\pi a^2} T \times \omega_{\dot\gamma - u_{\mathrm{BS}}}.$$

Note that the pipe flow component of $\omega_{\dot\gamma - u_{\mathrm{BS}}}$ is automatically annihilated by $T\times$. On the level of velocity, this adds momentum as

$$\Delta t \frac{C}{2\pi a^2} T \times (\dot\gamma - u_{\mathrm{BS}}) dm = \Delta t \frac{\rho C}{2} T \times (\dot\gamma - u_{\mathrm{BS}}) ds$$

and we arrive, accounting for the extra factor of 2 along the normal direction in $\langle\cdot,\cdot\rangle_{(1,2)}$, at Eq. (7).

D NUMERICAL IMPLEMENTATION DETAILS

D.1 Biot–Savart and Normal Flow

We adopt the 4^{th}-order Runge–Kutta method to evolve the ODE of Eq. (18). This only requires evaluation of the right-hand side for a polygonal curve γ, the individual components of which are elaborated in the following sections.

D.1.1 Evaluation of the Thickness. Let $\gamma^{(0)}$ be the initial polygonal curve given at the current time step, equipped with thickness $a_j^{(0)}$ on the edges $j \in E$. Then any of its deformations γ can be assigned thickness as

$$a_j := a_j^{(0)} \sqrt{\frac{\Delta s_j}{\Delta s_j^{(0)}}}$$

where $\Delta s_j^{(0)}$ and Δs_j are the length of edge j of $\gamma^{(0)}$ and γ respectively. Note that this conserves the volume of each edge.

D.1.2 Evaluation of the Normal Flow. The last two terms of Eq. (18) are evaluated on each edge, where a_j and T_j are both defined, followed by averaging (weighted by edge lengths) to vertices.

D.1.3 Evaluation of the Biot–Savart Velocity. This is done by integrating the Rosenhead–Moore kernel

$$u_{\mathrm{BS}}(s) = \frac{C}{4\pi}\int_{\mathbb{S}^1} \frac{T(\tilde s)\times(\gamma(s)-\gamma(\tilde s))}{\left(|\gamma(s)-\gamma(\tilde s)|^2 + \mu_{\mathrm{RM}}^2 a^2\right)^{3/2}} d\tilde s$$

where the Rosenhead–Moore constant $\mu_{\mathrm{RM}} = e^{-3/4}$ corresponds to uniform core [Saffman 1992, pp. 213]. With γ being a polygonal curve with straight edges , the integral is explicitly evaluated as a sum over edges [Weißmann and Pinkall 2010]

$$u_{\mathrm{BS}}^{\mathrm{disc}}(s) = \frac{C}{4\pi}\sum_j \left(\frac{\langle r_{j+1/2}, T_j \Delta s_j\rangle}{\sqrt{|r_{j+1/2}|^2 + \mu_{\mathrm{RM}}^2 a_j^2}} - \frac{\langle r_{j-1/2}, T_j \Delta s_j\rangle}{\sqrt{|r_{j-1/2}|^2 + \mu_{\mathrm{RM}}^2 a_j^2}}\right) \cdot \frac{r_{j-1/2}\times r_{j+1/2}}{(\Delta s_j)^2 \mu_{\mathrm{RM}}^2 a_j^2 + |r_{j-1/2}\times r_{j+1/2}|^2}$$

where $r_{j\pm 1/2} = \gamma_{j\pm 1/2} - \gamma(s)$, and $j + 1/2$ refers to the vertex incident on edges j and $j+1$. However, the polygonal approximation to the smooth curve removes the contribution of the cross product $T(\tilde s)\times(\gamma(s)-\gamma(\tilde s))$ on the immediate neighboring edges $j-1, j$. The missing integral over $[s-\Delta s_{j-1}, s+\Delta s_j]$ can be approximated by the localized induction given by

$$u_{\mathrm{LIA}} = -\frac{C}{4\pi}\log\left(\frac{\sqrt{\Delta s_{j-1}\Delta s_j}}{\delta_{\mathrm{RM}}\sqrt{a_{j-1}a_j}}\right) T \times \frac{dT}{ds}$$

where $\delta_{\mathrm{RM}} = \frac{1}{2}e^{1/4}$ and $T\times\frac{dT}{ds}$ is approximated by

$$2\frac{T_{j-1}\times T_j}{\Delta s_{j-1} + \Delta s_j},$$

the exact value of $T\times\frac{dT}{ds}$ for the interpolated curve being a circle circumscribing three consecutive vertices incident to edges $j-1$ and j. Putting everything together, our evaluation of the Biot–Savart velocity is given by

$$u_{\mathrm{BS}} = u_{\mathrm{BS}}^{\mathrm{disc}} + u_{\mathrm{LIA}}.$$

D.2 Discrete Burgers' Equation

We discretize the Burgers' equation by the finite volume method of Godunov [1959] (see [LeVeque 2002, Ch. 12]). First we identify Eq. (15) as a conservation law equation for A

$$\partial_t^E A = -\partial_s \varphi + \frac{C^2}{64\pi^2\nu}\partial_s^2 A \tag{22}$$

with the flux function

$$\varphi = \varphi(A,T) = \frac{\langle g, T\rangle}{8\pi\nu}A^2.$$

In the discrete setting the given data A_j is associated with edges and we want to solve for an updated $(A_j^*)_j$ representing the result of integrating Eq. (22) over a timespan Δt. To do so, define the discrete Laplace operator L (a symmetric negative-semidefinite sparse matrix) by

$$(LA)_j := 2\frac{A_{j+1}-A_j}{\Delta s_j + \Delta s_{j+1}} - 2\frac{A_j - A_{j-1}}{\Delta s_{j-1} + \Delta s_j}, \tag{23}$$

which approximates the integral of $\partial_s^2 A\, ds$ over the edge j. Integrating Eq. (22) over the edge j and adopting the Crank–Nicholson scheme for time integration, we have

$$\frac{\Delta s_j}{\Delta t}(A_j^* - A_j) = \underbrace{\varphi_{j-1/2} - \varphi_{j+1/2}}_{=:-\Delta\varphi_j} + \frac{C^2}{64\pi^2\nu}\left(L\frac{A^* + A}{2}\right)_j \tag{24}$$

where the half index $j + 1/2$ as before denotes the vertex shared by edges j and $j + 1$. The numerical flux $\varphi_{j+1/2}$ is evaluated using the existing data on the neighboring edges

$$\varphi_{j+1/2} = \Phi(A_j, T_j; A_{j+1}, T_{j+1}), \tag{25}$$

and the discrete flux function Φ respects the directions of the characteristic velocities $\partial_A \varphi(A, T)$ on the neighboring edges

$$\Phi(A_-, T_-; A_+, T_+) := \begin{cases} \frac{\langle g, T_-\rangle}{8\pi\nu} A_-^2, & \langle g, T_-\rangle A_- > \max\{0, -\langle g, T_+\rangle A_+\} \\ \frac{\langle g, T_+\rangle}{8\pi\nu} A_+^2, & \langle g, T_+\rangle A_+ < \min\{0, -\langle g, T_-\rangle A_-\} \\ 0, & \text{otherwise.} \end{cases}$$

In practice Eq. (24) is rearranged to the linear system

$$\left(M - \frac{C^2}{64\pi^2\nu}\frac{\Delta t}{2}L\right)A^* = -\Delta t\Delta\varphi + \left(M + \frac{C^2}{64\pi^2\nu}\frac{\Delta t}{2}L\right)A \tag{26}$$

where $M := \mathrm{diag}(\Delta s_j)$.

Algorithm 2 Discrete Burgers' Equation (Tangential Flow)

Input: Cross sectional areas A_j over edges of a polygonal curve γ with circulation C.

1: Compute edge lengths Δs_j and tangents T_j of γ.
2: Build L (Eq. (23)) and $M = \mathrm{diag}(\Delta s_j)$.
3: Compute $\varphi_{j+1/2}$ on vertices. ▷ Eq. (25).
4: Solve Eq. (26). ▷ Alternatively Eq. (27) or Eq. (28).

Output: Updated cross sectional areas A_j^*.

D.2.1 Volume Conservation. To see that the total volume is conserved note that $\sum_j \varphi_{j-1/2} - \varphi_{j+1/2} = 0$ since it is a telescoping sum. Similarly, from Eq. (23) it follows that $\sum_j (LA)_j = 0$. Thus the sum of Eq. (24) over all edges leads to conservation of total volume $\sum_j A_j^* \Delta s_j = \sum_j A_j \Delta s_j$.

D.2.2 Small Viscosity Large Circulation Limit. The Crank–Nicholson time step in Eq. (26) is accurate only when $\frac{C^2}{64\pi^2\nu} \ll \frac{\Delta s^2}{\Delta t}$. For large $\frac{C^2}{64\pi^2\nu}$, *e.g.*, for bubble rings, we use the backward Euler scheme

$$\left(M - \frac{C^2\Delta t}{64\pi^2\nu}L\right)A^* = -\Delta t\Delta\varphi + MA. \tag{27}$$

Note that $\frac{C^2}{64\pi^2\nu}$ is the diffusion term (right-hand side) of Eq. (15). When $\frac{C^2}{64\pi^2\nu} \gg \frac{\Delta s^2}{\Delta t}$ the thickness quickly relaxes to the steady state Eq. (16)

$$\frac{C^2}{64\pi^2\nu}LA^* = \Delta\varphi, \tag{28}$$

which is the limiting case $t \to \infty$ of Eq. (27).

D.3 Integration of Circulation

Writing the circulation equation (Eq. (12b)) as

$$\dot{C} = \underbrace{\frac{4\pi\mu}{U}\int_{\mathbb{S}^1}\langle \hat{u}_{\mathrm{BS}}, \dot{\gamma} - u_{\mathrm{BS}}\rangle_{(1,2)} ds}_{=:f(C)} - \underbrace{\frac{2\mu}{U}\int_{\mathbb{S}^1}\frac{1}{a^2}ds}_{=:k} C$$

where the dependency of f on C is in $\dot{\gamma} - u_{\mathrm{BS}}$, we update the circulation by an approximated integral $C^* \approx C(\Delta t)$ given the initial condition $C(0) = C_0$ of the present iteration. We approximate the nonlinear term $f(C)$ by the explicit constant $f(C_0)$ and integrate the remaining linear ODE exactly

$$\begin{aligned} &\dot{C} = -kC + f(C_0) \\ \Longrightarrow\quad &C^* = e^{-k\Delta t}C_0 + (1 - e^{-k\Delta t})\frac{f(C_0)}{k} \\ &\quad = e^{-k\Delta t}C_0 + (1 - e^{-k\Delta t})\frac{2\int_{\mathbb{S}^1}\langle \hat{u}_{\mathrm{BS}}, \dot{\gamma} - u_{\mathrm{BS}}\rangle_{(1,2)} ds}{\int_{\mathbb{S}^1}\frac{1}{A}ds}. \end{aligned}$$

To evaluate the normalized Biot–Savart energy U involved in evaluating k, we adopt [Weißmann and Pinkall 2010, App. A]. All integrals over $\mathbb{S}^1$ are evaluated by sums over edges.

D.4 Resampling and Topological Changes

D.4.1 Resampling. To maintain a quality discretization of the deforming space curve it must be resampled. At the end of each main iteration (Alg. 1) positions γ_i and cross sectional areas A_j are interpolated with the aid of splines. New vertex positions as well as corresponding edge values of A are then sampled to ensure that γ is well represented as it deforms.

D.4.2 Reconnection. Vortex filament reconnections are prominent events in bubble ring dynamics. We adopt a variant of the method of [Weißmann and Pinkall 2010] to reconnect long antiparallel vortex filaments (see inset). In this approach the reconnection criterion is a tradeoff between shorter filament length and the physical energy required for the reconnection event. Weissmann and Pinkall check this criterion over all pairs of edges i, j, whereas we check the same criterion over pairs of curve segments $(i, i+1, \ldots, i+m_i), (j, j+1, \ldots, j+m_j)$ with a fixed physical length. This improves the discretization independence in reconnection.

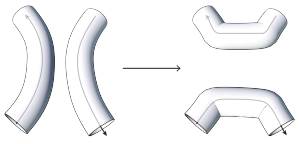

D.4.3 Droplet Formation. In the case of ink filaments, the relatively large viscosity eventually leads to small circulation (Eq. (12b)). In effect the diffusion term in the Burgers' equation plays less of a regularizing role, resulting in the thick segments cumulating at the local minima of the height $\langle \frac{g}{|g|}, \gamma\rangle$. These segments rush down driven by the term $\frac{16\pi^2\nu a^2}{256\pi^2\nu^2 + C^2} g^\perp$ which is proportional to the thickness

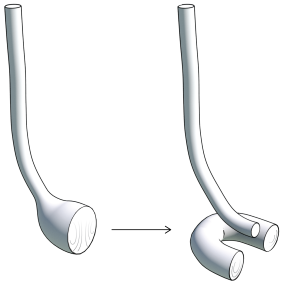

a^2. Beyond a threshold the fast normal motion of the curve forms a new vortex ring (see inset).

In practice, we adopt a heuristic criterion to identify curve segments with large $|\dot{\gamma}^\perp|$ by comparing it with the median value over the filament. Each of these segments is converted into a new vortex ring with an assigned circulation C proportional to the quantity $a|\dot{\gamma}^\perp|$ (which has a matching dimension) of the original filament. The new vortex ring has thickness and radius (offset) proportional to a of the original filament.

E STOKES FLOW FOR A DEFORMING BODY

We treat our filaments as full tori $M_1 \in \mathbb{R}^3$ changing shape and position in time. This is captured by the normal velocity of ∂M_1. Since all vorticity is contained in M_1 the velocity u in the exterior M_0 is fully determined by the Neumann data $\langle u, N\rangle$ on ∂M_1 induced by $\dot{\gamma}$, the $\operatorname{div} u = 0$ and $\operatorname{curl} u = 0$ constraints, and the circulation C around γ. The flow on the inside of the filament is assumed to be Stokes [Childress 2009, Ch. 7] (see also [Lauga and Powers 2009] for additional intuition). We therefore take u inside M_1 to be the unique Stokes flow compatible with the Dirichlet boundary data of u in the exterior. We now prove that this flow exists and is unique. No doubt this is a known fact, but we could not find a proof in the literature.

Lemma E.1 (Stokes flow as boundary value problem). *For any boundary data $u_\partial \in L^2(\partial M_1;\mathbb{R}^3)$ with $\int_{\partial M_1}\langle u_\partial, N\rangle dA = 0$ (net zero flux), the Stokes equation*

$$\Delta u = \operatorname{grad} w, \quad \operatorname{div} u = 0, \quad u|_{\partial M_1} = u_\partial$$

has a unique weak solution $u \in W^{1,2}(M_1;\mathbb{R}^3)$ with $w \in L^2(M_1;\mathbb{R})$. That is, there exists a unique u in the affine space $V_{u_\partial} := \{u \in W^{1,2}(M_1;\mathbb{R}^3) \mid \operatorname{div} u = 0, u|_{\partial M_1} = u_\partial\}$ such that

$$\langle\!\langle \operatorname{curl} u, \operatorname{curl} \xi\rangle\!\rangle = \langle\!\langle w, \operatorname{div} \xi\rangle\!\rangle \quad \text{for all } \xi \in W_0^{1,2}(M_1;\mathbb{R}^3), \tag{29}$$

where $\langle\!\langle\cdot,\cdot\rangle\!\rangle$ is the L^2 inner product on M_1.

Note that the Stokes equation in weak form Eq. (29) is also the Euler-Lagrange equation for minimizing the dissipation $\|\operatorname{curl} u\|^2$ under the constraints $\operatorname{div} u = 0$ and $u|_{\partial M_1} = u_\partial$.

Proof of Lemma E.1. Using the fact that $\operatorname{div}\colon W_0^{1,2}(M_1;\mathbb{R}^3) \to L^2(M_1;\mathbb{R})$ is surjective, a bounded linear functional f on $W_0^{1,2}(M_1;\mathbb{R}^3)$ vanishing on $\ker(\operatorname{div})$ implies that there is a bounded linear functional $g = \langle\!\langle w, \cdot\rangle\!\rangle$ on $L^2(M_1;\mathbb{R})$ such that $f = g \circ \operatorname{div}$. Therefore it is enough to show that there exists a unique $u \in V_{u_\partial}$ such that $\langle\!\langle \operatorname{curl} u, \operatorname{curl} \xi\rangle\!\rangle = 0$ for all $\xi \in V_0 := W_0^{1,2}(M_1;\mathbb{R}^3) \cap \ker(\operatorname{div})$.

Now, consider $H = W^{1,2}(M_1;\mathbb{R}^3) \cap \ker(\operatorname{div})$ in which V_0 is a subspace and V_{u_∂} is an affine space parallel to V_0. Define an inner product $\langle\!\langle \xi, \eta\rangle\!\rangle_H = \langle\!\langle \operatorname{curl} \xi, \operatorname{curl} \eta\rangle\!\rangle + \int_{\partial M_1}\langle \xi|_{\partial M_1}, \eta|_{\partial M_1}\rangle dA$, which makes H into a Hilbert space. Here we used the fact that there is no nontrivial harmonic field ($\ker(\operatorname{div}) \cap \ker(\operatorname{curl})$) that vanishes on the boundary. Then by the Hilbert projection theorem there is a unique orthogonal projection u of $0 \in H$ onto the affine space V_{u_∂}. In particular $u \perp V_0$ with respect to $\langle\!\langle\cdot,\cdot\rangle\!\rangle_H$. That is, $\langle\!\langle \operatorname{curl} u, \operatorname{curl} \xi\rangle\!\rangle = 0$ for all $\xi \in V_0$. □